J. Fluid Mech. (2013), *vol.* 730, *pp.* 52–75.
doi:10.1017/jfm.2013.335

Relationship between aerodynamic forces, flow structures and wing camber for rotating insect wing planforms

R. R. Harbig†, J. Sheridan and M. C. Thompson

Fluids Laboratory for Aeronautical and Industrial Research (FLAIR), Department of Mechanical and Aerospace Engineering, Monash University, Clayton, VIC 3800, Australia

(Received 7 March 2013; revised 24 May 2013; accepted 24 June 2013;
first published online 30 July 2013)

Wing deformation is observed during the flight of some insect species; however, the effect of these distorted wing shapes on the leading edge vortex (LEV) is not well understood. In this study, we investigate the effect of one of these deformation parameters, (rigid) wing camber, on the flow structures and aerodynamic forces for insect-like wings, using a numerical model of an altered fruit fly wing revolving at a constant angular velocity. Both positive and negative camber was investigated at Reynolds numbers of 120 and 1500, along with the chordwise location of maximum camber. It was found that negatively cambered wings produce very similar LEV structures to non-cambered wings at both Reynolds numbers, but high positive camber resulted in the formation of multiple streamwise vortices at the higher Reynolds number, which disrupt the development of the main LEV. Despite this, positively cambered wings were found to produce higher lift to drag ratios than flat or negatively cambered wings. It was determined that a region of low pressure near the wing's leading edge, combined with the curvature of the wing's upper surface in this region, resulted in a vertical tilting of the net force vector for positively cambered wings, which explains how insects can benefit from wing camber.

Key words: biological fluid dynamics, swimming/flying

1. Introduction

Research into the aerodynamics of insect flight has found that a stable leading edge vortex (LEV) is a common flow feature that provides insect wings with additional circulation and enhanced lift (Ellington *et al.* 1996; Usherwood & Ellington 2002; Birch, Dickson & Dickinson 2004). Wing deformation is observed during the flight of some insect species (e.g. Weis-Fogh 1973; Wootton 1981; Ellington 1984) and is a result of the wing's passive response to inertial and aerodynamic forces during flight. Wing deformation is observed as wing twist, camber and spanwise bending. Most investigations into the flow around flapping and rotating wings have been performed under the assumption that the wing is rigid and flat, and consequently, the effect of these wing deformations on the LEV is still unclear.

† Email address for correspondence: robert.harbig@monash.edu

Of particular interest is the chordwise bending of the wing that produces either a convex shape (positive camber) or a concave shape (negative camber) of the wing's top surface. For conventional aircraft with attached flow, positive wing camber is generally advantageous. However, for thin insect wings at high angles of attack the flow separates from the wing's leading edge and therefore conventional reasoning for camber does not apply to insect flight (Usherwood & Ellington 2002). Early studies into the effect of camber on insect wings had mixed results, where some found it to be beneficial (Jensen 1956; Vogel 1967), while others reported insignificant effects (Dickinson & Gotz 1993). These early studies ignored the effects of wing rotation but more recent studies have shown that the wing's rotation is important for insect flight (Ellington *et al.* 1996; Dickinson, Lehmann & Sane 1999; Lentink & Dickinson 2009). Wing rotation results in a highly three-dimensional LEV structure and generates a strong spanwise flow from the wing's root to tip (Birch & Dickinson 2001; Birch *et al.* 2004; Lentink & Dickinson 2009). This spanwise flow is thought to help stabilize the LEV to the wing's surface by draining circulation out into the tip vortex (Ellington *et al.* 1996; Lentink & Dickinson 2009).

Usherwood & Ellington (2002) were the first to investigate the use of camber for a rotating insect wing. They found that camber did not have a measurable effect on the aerodynamic forces. In contrast, later rotating and flapping wing studies have shown that positive camber increases the aerodynamic performance of the wing (Altshuler, Dudley & Ellington 2004; Tsuzuki, Sato & Abe 2007; Du & Sun 2008; Young *et al.* 2009; Gopalakrishnan & Tafti 2010; Nakata & Liu 2012*a*,*b*), while flexible wings that create negative camber degrade the wing's lift (Zhao *et al.* 2010). However, despite the importance of the LEV for flapping flight, few studies have investigated the effect of wing camber on the vortex structures around a flapping or rotating wing. Zhao, Deng & Sane (2011*a*,*b*) showed that the degree of trailing edge flexion strongly correlates with the magnitude of vorticity at the leading edge. Du & Sun (2008) suggest that the LEV is distorted by positive wing camber, but details of what this distortion entails is omitted. Therefore a more thorough investigation is required into the effect of wing camber on the structure of the LEV in order to understand how it influences the aerodynamic forces.

This paper describes an investigation into the effect of wing camber on impulsively started rotating wings at insect Reynolds numbers. A generic fruit fly wing is numerically modelled as a rigid wing with varying magnitudes of camber. The effects of both positive and negative camber on the aerodynamic forces and flow structures are investigated, as well as the effect of the chordwise location of maximum camber. These results reveal how changes in the wing's shape result in a significant alteration of the LEV's structure at a Reynolds number of 1500. The impact that this modified LEV structure has on the aerodynamic forces, in combination with the change in wing shape, is then discussed. The effect of camber at a Reynolds number of 120 is also investigated, and it is shown that the mechanism through which camber improves the wing's performance is the same at this lower Reynolds number as at the higher value. In particular, it is due to tilting of the force vector as the camber is increased.

2. Numerical method

The flow over a revolving wing is modelled by the Navier–Stokes equations cast in a non-inertial rotating frame of reference and combined with the continuity constraint,

$$\frac{\partial \rho \boldsymbol{u}_{abs}}{\partial t} + \boldsymbol{\nabla} \cdot (\rho \boldsymbol{u} \boldsymbol{u}_{abs}) = -\boldsymbol{\nabla} p + \boldsymbol{\nabla} \cdot \boldsymbol{\tau} - \rho \boldsymbol{\Omega} \times \boldsymbol{u} - \rho \boldsymbol{\Omega} \times (\boldsymbol{\Omega} \times \boldsymbol{r}), \tag{2.1}$$

and

$$\nabla \cdot \boldsymbol{u} = 0. \tag{2.2}$$

Here, ρ is the fluid density, $\boldsymbol{u}$ and $\boldsymbol{u}_{abs}$ are the velocity vectors in rotating and absolute frames respectively, p is the pressure, $\boldsymbol{\Omega}$ is the rotational velocity vector, $\boldsymbol{r}$ is the location vector and $\boldsymbol{\tau}$ is the stress tensor, which is defined as

$$\boldsymbol{\tau} = \mu(\nabla \boldsymbol{u} + (\nabla \boldsymbol{u})^T - \tfrac{2}{3}\boldsymbol{I}\nabla \cdot \boldsymbol{u}), \tag{2.3}$$

where μ is the fluid viscosity and $\boldsymbol{I}$ is the identity matrix. The last two terms in (2.1) are the Coriolis and centrifugal momentum source terms due to the rotating frame. In order to minimize numerical error an alternative rotation model was used, whereby the velocity in the advection and transient terms is modified to involve the absolute frame velocity rather than the relative frame velocity, hence the use of $\boldsymbol{u}_{abs}$ in (2.1). The angular acceleration of the fluid is included in the transient term as $\boldsymbol{u}_{abs} = \boldsymbol{u} + \boldsymbol{\Omega} \times \boldsymbol{r}$. These equations were solved directly using the commercial finite-volume-based code ANSYS CFX. The formally second-order accurate specified blend factor scheme (with $\beta = 1$) was used for spatial discretization and a second-order backward Euler scheme for the time evolution terms.

A real insect wing's camber varies throughout the course of the flapping cycle and can also vary along the wing's length (Walker, Thomas & Taylor 2009, 2010) due to the complex interaction of the wing's structural properties with the forces induced from the wing's kinematics. In order to isolate the effect on the aerodynamic forces and flow structures due to the wing's shape, we defined the wing as being rigid with constant camber along its span. The wing's motion was also simplified to an impulsively started rotational motion. These two simplifications deviate from real insect flight, but allowed us to eliminate the effects of the wing's structure and kinematics.

The wing was modelled as a rigid plate with square edges with a thickness of 3 % of the mean chord. The planform shape was based on a generic fruit fly wing (*Drosophila melanogaster*). This planform was chosen as it has been studied extensively both computationally (Aono, Liang & Liu 2008; Kweon & Choi 2010) and experimentally (Birch & Dickinson 2001; Birch *et al.* 2004; Poelma, Dickson & Dickinson 2006; Lentink & Dickinson 2009). The wing was scaled to have a wing span of 2.47 mm and an aspect ratio of 2.91, similar to that of an actual fly's wing (Zanker & Gotz 1990). The wing's camber was defined by the equations for the mean camber line (y_c) of a NACA four-digit wing section,

$$y_c = \begin{cases} \dfrac{m}{p^2}(2px_c - x_c^2), & x_c \leqslant p, \\ \dfrac{m}{(1-p)^2}[(1-2p) + 2px_c - x_c^2], & x_c > p, \end{cases} \tag{2.4}$$

where m is the maximum ordinate of the camber line, p is the chordwise position of the maximum ordinate and x_c is the abscissa of a point on the chord line. This equation was applied locally along the wing's span in order to maintain the same planform shape between each wing. The magnitude of camber was varied in the interval $-0.15 \leqslant m/c \leqslant 0.2$ and three chordwise positions of maximum camber were considered, $p/c = 0.25, 0.5$ and 0.75. An example of a cambered fruit fly wing used in this study as well as the coordinate system used in the computations is shown in figure 1.

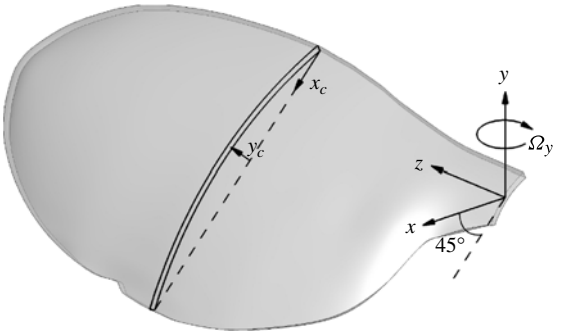

FIGURE 1. Schematic of the coordinate system and fly wing geometry with $m/c = 0.1$ and $p/c = 0.5$.

Each wing was prescribed a simplified kinematic motion to simulate the vortex structures that are formed during the mid-stroke of a typical insect flapping cycle without the complication of wing rotation and reversal found at the end of each half-stroke. The kinematic motion consisted only of a rotation about the wing's base (y-axis) at a constant angle of attack (α) of 45°. The wing was initially at rest and was accelerated over a period of $t = 0.084T$ before rotating at a constant rotational velocity Ω. An impulsively started wing rotating about its base has been shown to be a good approximation to the beginning of a typical insect flapping cycle (Poelma *et al.* 2006; Lentink & Dickinson 2009). This kinematic motion is described by (2.5), where T is the total simulation time:

$$\Omega_y(t) = \begin{cases} \dfrac{1}{2}\Omega\left(1 - \cos\left(\dfrac{\pi t}{0.084T}\right)\right), & t < 0.084T, \\ \Omega, & t \geqslant 0.084T. \end{cases} \tag{2.5}$$

The simulation was stopped after the angle through which the wing had rotated (ϕ) had reached 270°. As will be shown in § 3.2, this allowed ample time for a quasi-steady flow state to form. For consistency with previous studies, the Reynolds numbers (Re) used here were 120 and 1500, and were calculated using the velocity at the radius of gyration ($U_{rg} = 2.186$ m s^{-1}) and the mean chord length. Harbig, Sheridan & Thompson (2013) have shown, however, that the wing span is a more appropriate length scale to use, particularly if the wing's aspect ratio is varied. The fluid's viscosity was adjusted in order to achieve the desired Reynolds numbers without changing the wing's kinematics.

The wing was located in the centre of a cylindrically shaped computational domain whose axis was coincident with the rotation axis of the wing, whose diameter was 18 times the wing span, and whose length was 48 times the average wing chord. The boundary condition on the outer cylindrical surface was a free-slip wall condition ($U_n = 0$), while for the top and bottom circular surfaces fluid was allowed to flow into and out of the domain with the average pressure on each boundary held at zero gauge pressure. A no-slip boundary condition was applied at the wing's surface.

The computational domain was meshed using an unstructured tetrahedral mesh with a region of triangular prism elements near the wing's surface. The effects of spatial resolution were explored using a flat non-cambered wing. Three grids were generated such that the element size on the wing's surface and in the surrounding fluid zones were successively halved. The calculated aerodynamic force coefficients for each mesh

Mesh	Surface size	Elements (million)	C_L	GCI (%)	C_D	GCI (%)
1	$0.02857\bar{c}$	1.538	1.834	0.286	1.719	1.51
2	$0.01449\bar{c}$	5.490	1.837	0.102	1.701	0.177
3	$0.00725\bar{c}$	27.36	1.838	0.028	1.699	0.012

TABLE 1. Mesh resolution study

are shown in table 1. The *grid convergence index* (GCI) method was used to estimate the numerical error (Roache 1998). Mesh 3 had a GCI of less than 0.03 % and was selected for this study. The temporal error was estimated in a similar way and was found to have a GCI of 0.68 % for C_L and C_D with a time step of $0.00185T$.

The results of this model were validated against the flow visualizations of Lentink & Dickinson (2009). These results are compared in a previous study by Harbig *et al.* (2013), and show good agreement of the LEV and tip vortex structures with the experimental flow visualizations at two Reynolds numbers. In addition, the variation in the aerodynamic forces throughout the simulation are also compared to the experimental measurements of Birch *et al.* (2004) in § 3.1 below.

3. Results and discussion

3.1. *Aerodynamic forces*

The lift and drag coefficients used in this study are calculated as $C_L = 2L/\rho U_{rg}^2 S$ and $C_D = 2D/\rho U_{rg}^2 S$ respectively, where S is the wing area and L and D are the aerodynamic forces acting in the y and x directions respectively. The variation of the lift and drag coefficients with time at a Reynolds number of 1500 for different magnitudes of wing camber are shown in figure 2 along with the experimental force measurements of Birch *et al.* (2004) for a flat non-cambered wing. Here it should be noted that the current CFD model is not intended to be an exact replica of their experiment. Nonetheless, the variation of the aerodynamic force is consistent with previously reported aerodynamic forces for impulsively started rotating wings (Dickinson *et al.* 1999; Birch *et al.* 2004), where there is an initial transient period in which the force coefficients reach a maximum, which is followed by a minimum, before the lift and drag coefficients recover and there is a period of approximately constant force production. The average lift coefficient over the period of steady force production for our 0 % camber wing is approximately 9 % lower than the average experimental lift coefficient and the mean drag coefficient is approximately 6 % higher. In addition, the maximum lift and drag coefficients are 12 and 3 % lower, respectively, than the maximum experimental values.

In these simulations, steady aerodynamic forces for the 0 % camber wing are produced from approximately $t = 0.36T$ or after the wing has rotated through 90°. Figure 2 shows that this point occurs significantly later for wings with negative camber (e.g. $t = 0.407T, \phi = 103°$ at −15 % camber) and slightly earlier for wings with positive camber (e.g. $t = 0.341T, \phi = 84°$ at 15 % camber). The estimated settling times and corresponding angles of rotation at different magnitudes of camber are shown in table 2. Figure 2 also shows that the 15 % camber wing produced not only higher lift coefficients during the period of steady lift production but it also produced a higher minimum lift coefficient and a slightly increased maximum lift coefficient. Conversely, the −15 % camber wing produced lower lift coefficients all round.

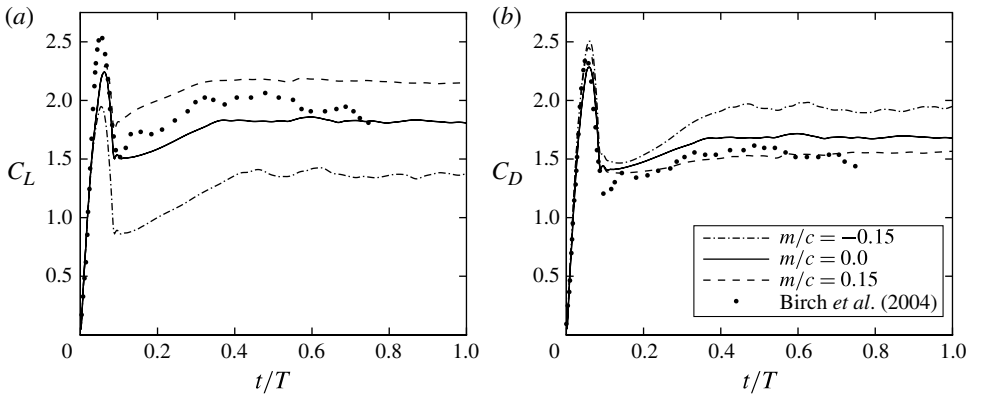

FIGURE 2. Time variation of the (*a*) lift coefficient and (*b*) drag coefficient throughout the simulation for −15, 0 and 15 % camber wings at $Re = 1500$. The experimental results of Birch *et al.* (2004) ($Re = 1400, \alpha = 40°$) are also included for comparison with the 0 % camber wing.

m/c	t/T	ϕ
−0.15	0.407	103
−0.10	0.391	98
−0.05	0.375	94
0	0.359	89
0.05	0.353	88
0.10	0.347	86
0.15	0.341	84
0.20	0.335	82

TABLE 2. Estimated settling times (t/T) and corresponding rotation angles (ϕ) for different magnitudes of camber (m/c)

Figure 3(*a*) shows the variation in the average lift and drag coefficients with camber, where the coefficients are the average values calculated over the period given by the values in table 2 to the end of the wing's rotation. Figure 3(*a*) shows that positively cambered wings have increased lift coefficients and decreased drag coefficients compared to a flat wing. On the other hand, negative camber has the opposite effect, reducing the lift coefficient and increasing the drag coefficient. We found that 15 % camber ($p/c = 0.5$) increased the wing's lift on drag ratio by 30.0 % compared to a flat wing, while −15 % camber ($p/c = 0.5$) reduced the lift on drag ratio by 34.5 % (see figure 3*b*). These results agree with the findings of Altshuler *et al.* (2004), Tsuzuki *et al.* (2007) and Du & Sun (2008), and show that positive wing camber could be used to improve aerodynamic performance of flapping and rotating wing micro air vehicles.

In addition, the chordwise location of the maximum camber was investigated and found to have a small influence on the wing's performance, particularly at high magnitudes of camber. For positively cambered wings, having the point of maximum camber located at the mid-chord was found to be optimum. For negatively cambered

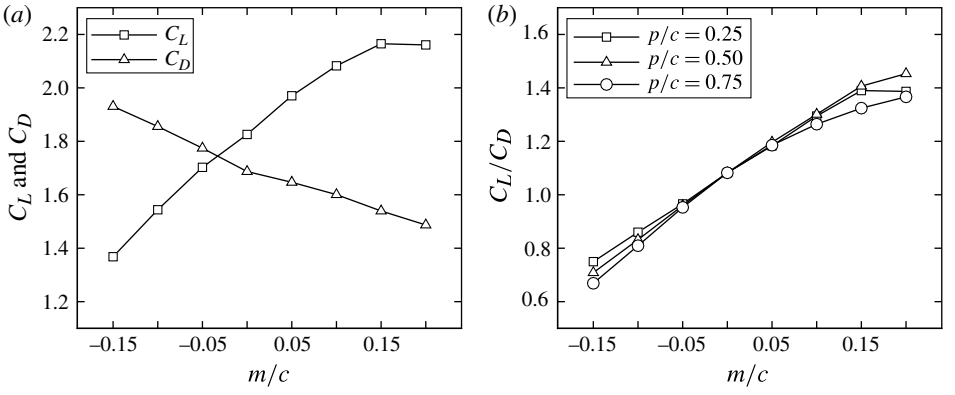

FIGURE 3. Average aerodynamic force graphs at $Re = 1500$. (*a*) Change in lift and drag coefficients with magnitude of camber, m/c (for $p/c = 0.5$). (*b*) Variation in lift on drag ratio with magnitude of camber for $p/c = 0.25$, 0.5 and 0.75.

wings, $p/c = 0.25$ produced the highest lift on drag ratios, with degrading performance as the location of maximum camber moves towards the wing's trailing edge.

3.2. *Flow structures*

3.2.1. *Negative camber*

In this section we first look at the vortex structures that are formed around a non-cambered wing. At this Reynolds number ($Re = 1500$), a rigid wing with no camber produces a dual co-rotating LEV structure. This dual LEV structure is shown in figure 4(*a*) and consists of two co-rotating vortices (labelled LEV 1 and 2) separated by a smaller counter-rotating vortex (labelled SV). LEV 1 follows the leading edge of the wing while LEV 2 moves away from the leading edge as it tracks out along the wing's span and eventually breaks down at approximately 60 % span. A dual leading edge vortex structure has been observed by Srygley & Thomas (2002) over butterfly wings during wing beats that resulted in very large accelerations of the butterfly and has been shown to exist under certain Reynolds number conditions and angles of attack for a range of wing shapes (Lu, Shen & Lai 2006; Phillips, Knowles & Lawson 2010).

Negatively cambered wings were found to produce very similar vortex structures. Figure 4 shows the variation in the spanwise vorticity contours at $\phi = 270°$ with increasing negative camber. Here a dual co-rotating LEV structure can be seen on all the wings as depicted by the two distinct regions of negative vorticity near the leading edge. One notable difference in the LEV's structure between the negatively cambered wings is that LEV 2 breaks down closer to the wing's root as the wing becomes more negatively cambered. Vortex breakdown is an abrupt change in the structure of a vortex with a marked retardation of the flow in the axial direction (Hall 1972). The position of the breakdown point along the wing's span (r/R) as a function of the magnitude of camber is shown in figure 5, where the breakdown point is estimated as the point at which the spanwise velocity in the vortex core approaches zero.

The development of a dual LEV structure throughout the wing's motion for a flat non-cambered wing has been previously reported in Harbig *et al.* (2013) (see also supplementary movie 1 available at http://dx.doi.org/10.1017/jfm.2013.335). Perhaps unsurprisingly the development of the dual LEV structure over a negatively cambered

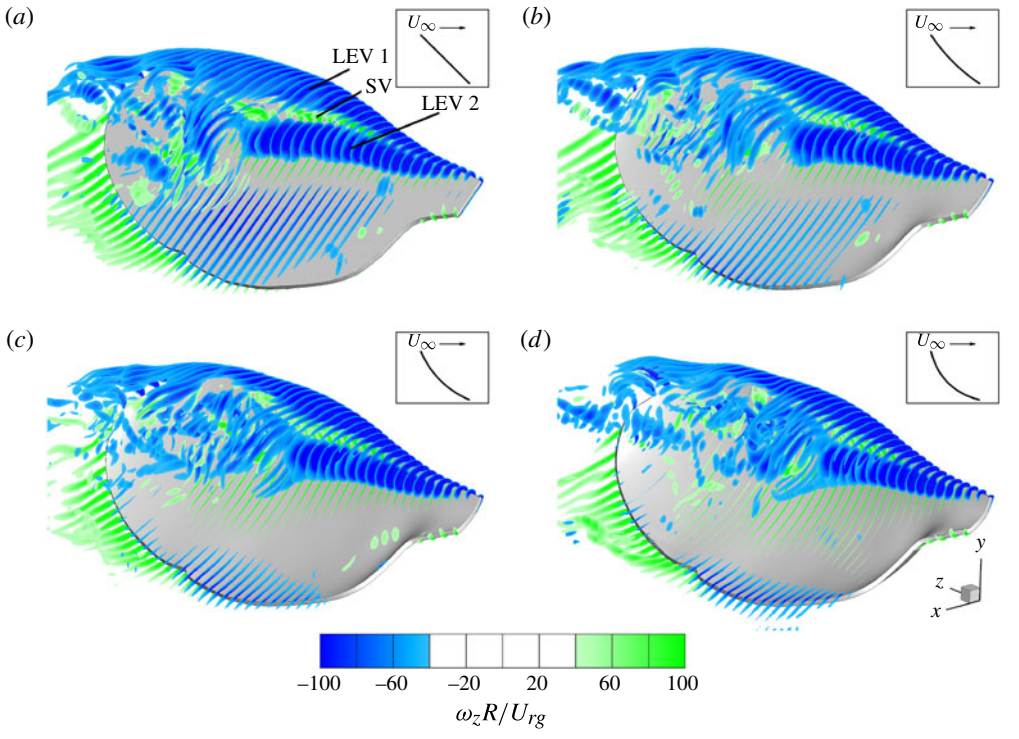

FIGURE 4. (Colour online) Change of spanwise vorticity contours ($\omega_z R/U_{rg}$) with decreasing magnitude of camber at $Re = 1500$: (*a*) 0 %, (*b*) −5 %, (*c*) −10 %, (*d*) −15 % ($p/c = 0.5$). The images show flow structures at $\phi = 270°$. The insets show a cross-sectional view of the wing's shape.

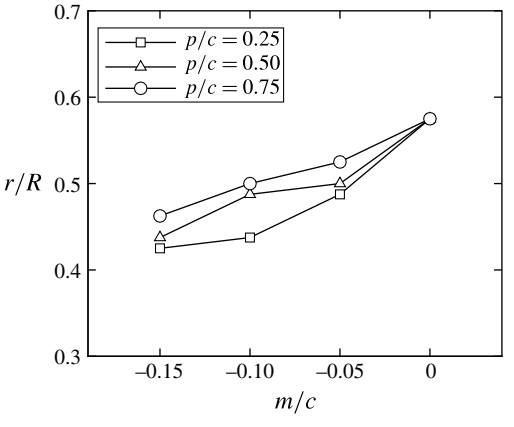

FIGURE 5. Spanwise position (r/R) of breakdown location as a function of the magnitude of camber (m/c).

wing is very similar to that for a flat wing. Figure 6 shows the time variation in surfaces of the Q criterion throughout the simulation for a −15 % cambered wing (see also supplementary movie 2). The Q criterion is the second invariant of the velocity gradient tensor (Hunt, Wray & Moin 1988) and is a measure of the magnitude of

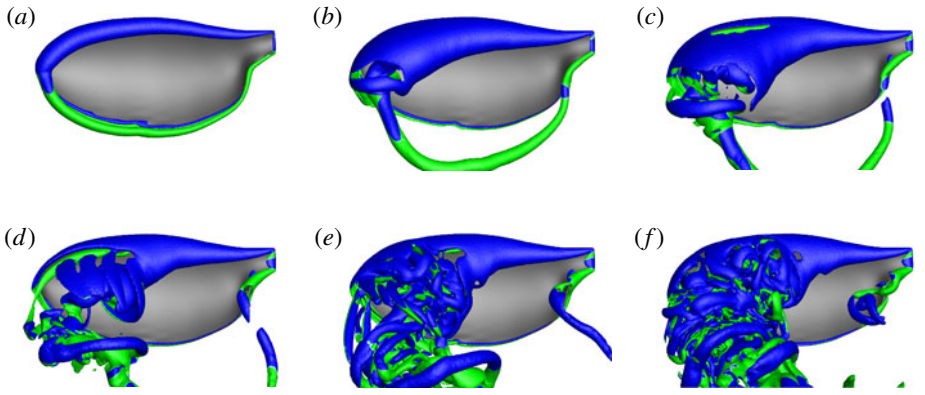

FIGURE 6. (Colour online) Temporal development of vortex structure over a −15 % camber wing ($p/c = 0.5, Re = 1500$): (*a*) $t/T = 0.081$, $\phi = 11.1°$; (*b*) $t/T = 0.178$, $\phi = 38.3°$; (*c*) $t/T = 0.267$, $\phi = 63.3°$; (*d*) $t/T = 0.363$, $\phi = 90.5°$; (*e*) $t/T = 0.467$, $\phi = 120°$; (*f*) $t/T = 0.681$, $\phi = 180°$. Vortex structures are visualized using surfaces of constant Q criterion and are coloured by spanwise vorticity (ω_z) to indicate direction: blue is negative and green is positive. The images show flow structures throughout the wing's rotation and are taken perpendicular to the wing's surface.

rotation rate relative to strain rate in a fluid. Positive values of Q represent areas where the local magnitude of rotation in the fluid dominates relative to strain and can therefore be used to highlight vortical structures. Figure 6 shows that at the beginning of the wing's motion a horseshoe-shaped vortex is formed, which consists of the LEV, tip vortex and trailing edge vortex. As the wing continues to rotate, the LEV grows in size and the trailing edge vortex is shed from the wing. The LEV enlarges more rapidly towards the wing tip, which results in a three-dimensional vortex structure. This flow structure development is similar to that computed for the initial part of the downstroke of a hovering fruit fly, honeybee and hawkmoth (Liu & Aono 2009). At $t/T = 0.267$ (figure 6*c*) the iso-Q surface representing the LEV begins to split in the outer part of the wing indicating that the dual LEV has formed. By $t/T = 0.363$ (figure 6*d*) LEV 2 has burst, resulting in smaller-scale structures being formed which are advected into the tip vortex as the wing's motion continues. Figure 6 shows that a quasi-steady state is reached for $0.363 \leqslant t/T \leqslant 0.467$, which corresponds to the settling time of $t/T = 0.407$ shown in table 2.

3.2.2. *Positive camber*

In contrast to wings with negative camber, positively cambered wings were found to dramatically influence the makeup of the LEV's structure. Increasing wing camber resulted in the initially coherent LEV becoming less distinct and the formation of multiple streamwise oriented vortex structures. The development of these vortex structures with increasing camber is shown in figure 7, where the vortices are visualized using surfaces of constant Q criterion. As described previously, for the flat wing (figure 7*a*) a dual co-rotating LEV structure forms over the wing. Increasing the wing's camber to 5 % results in a similar dual LEV structure. However, two small streamwise oriented vortex structures also form (labelled A and B in figure 7*b*). These structures originate from the wing's leading edge and appear to be entrained into LEV 2. A further increase in wing camber to 10 % results in these streamwise structures becoming more coherent and for a third streamwise vortex to be observed

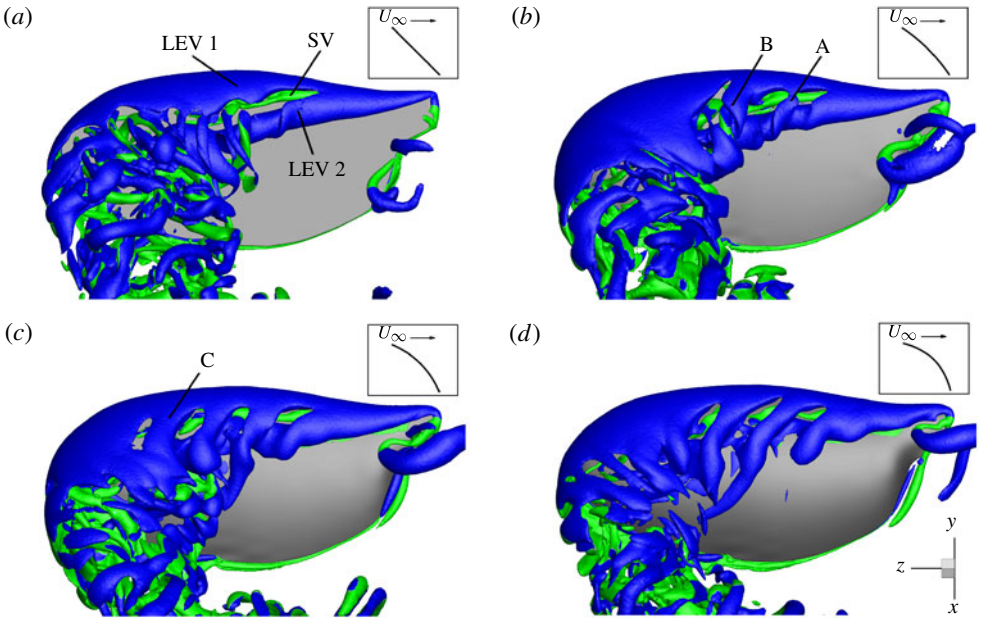

FIGURE 7. (Colour online) Change of vortex structures with increasing magnitude of camber at $Re = 1500$: (*a*) 0 %, (*b*) 5 %, (*c*) 10 %, (*d*) 15 % ($p/c = 0.5$). Vortex structures are visualized using surfaces of constant Q criterion and are coloured by spanwise vorticity (ω_z) to indicate direction: blue is negative and green is positive. The images show flow structures at $\phi = 270°$ and are taken perpendicular to the wing's surface. The insets show a cross-sectional view of the wing's shape.

(labelled C in figure 7*c*). All of these streamwise vortices feed into the tip vortex. At 15 % camber the streamwise vortices appear to dominate the flow topology and significantly inhibit the development of LEV 2 across the wing and at this point LEV 2 is now entrained into vortex A.

The change of the vortex structure over wings with increasing magnitude of camber is further highlighted in figure 8, which shows the change in both spanwise and streamwise vorticity patterns at 270° of rotation. For the non-cambered wing (figure 8*a*), two distinct regions of negative spanwise vorticity can be seen, signalling the presence of a dual LEV structure, where one is near the leading edge of the wing and the other is further downstream close to the wing's surface. Beyond approximately 60 % span the region of concentrated spanwise vorticity representing LEV 2 breaks up, indicating that LEV 2 has burst. The streamwise vorticity contours in figure 8(*b*) show a large region of negative vorticity over the inner part of the wing, close to the leading edge. Increasing the wing's camber to 5 % results in this region of negative streamwise vorticity beginning to split into three separate regions. Another weaker region of negative vorticity can also be seen to form closer to the wing tip, extending out from the wing's leading edge. As the wing's camber is increased from 5 to 15 %, two distinct regions of negative streamwise vorticity form over the middle portion of the wing (labelled A and B in figure 8*h*) and the region of negative streamwise vorticity near the wing tip strengthens (labelled C in figure 8*h*), resulting in three co-rotating streamwise vortices. The region of negative streamwise vorticity near the wing's root is also seen to reduce in size and strength.

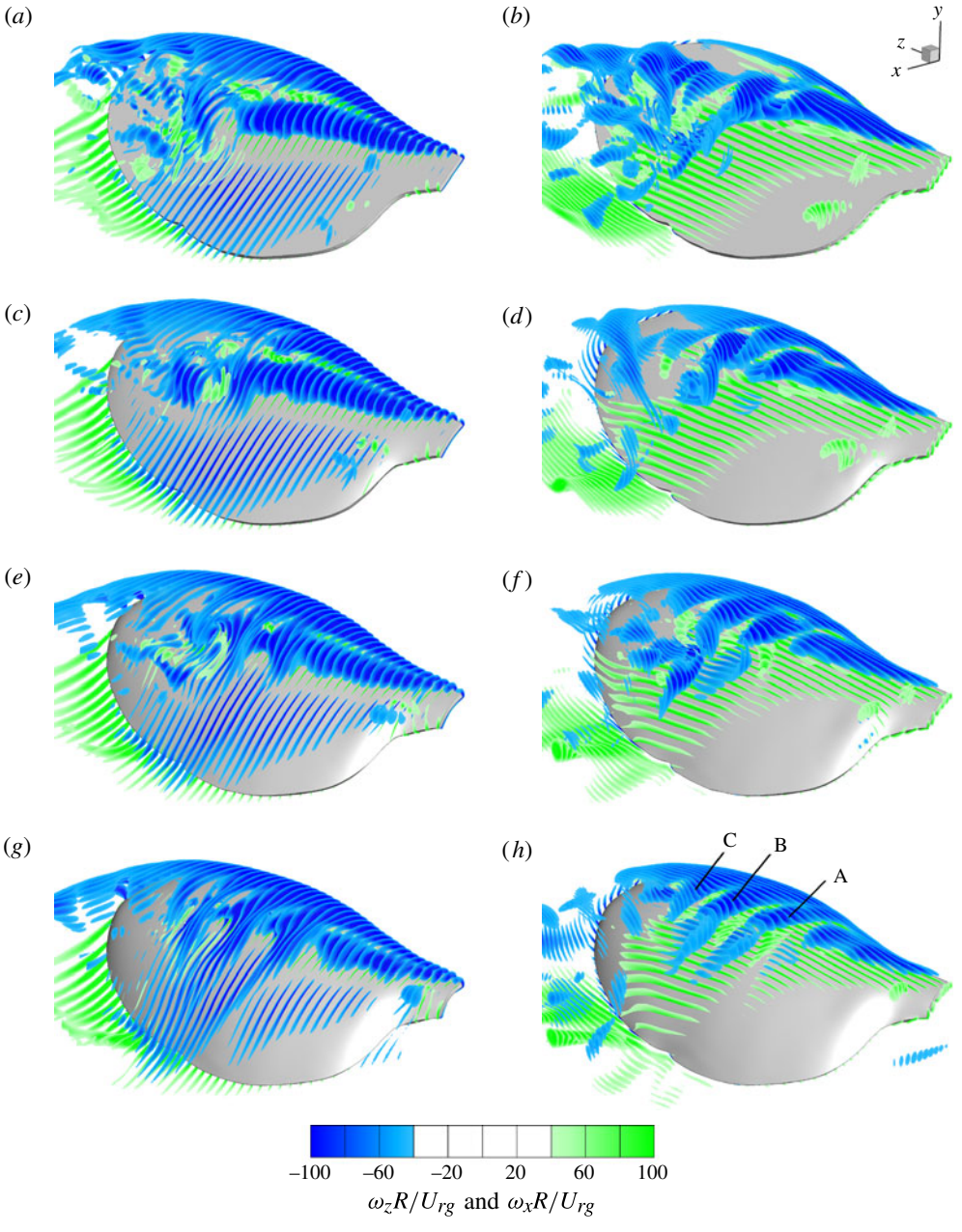

FIGURE 8. (Colour online) Change of spanwise vorticity contours ($\omega_z R/U_{rg}$, *a,c,e,g*) and streamwise vorticity contours ($\omega_x R/U_{rg}$, *b,d,f,h*) with increasing magnitude of camber at $Re = 1500$: (*a,b*) 0 %, (*c,d*) 5 %, (*e,f*) 10 %, (*g,h*) 15 % ($p/c = 0.5$). The images show flow structures at $\phi = 270°$.

As these streamwise vortices form, they begin to influence the development of LEV 2 as it extends across the wing. At 5 % wing camber (figure 8*c*) the spanwise vorticity contours for LEV 2 are distorted slightly around the wing's mid-span. Increasing the camber to 10 and 15 % results in further distortion and stretching of

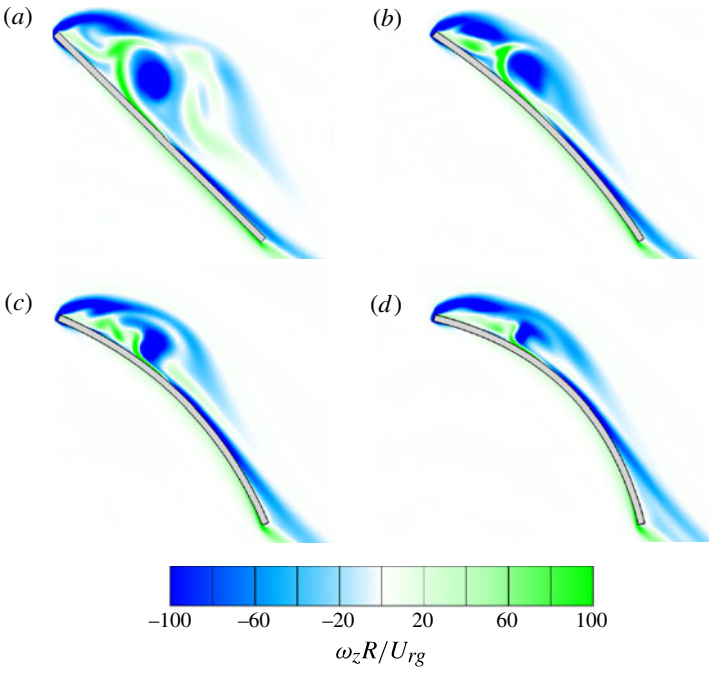

FIGURE 9. (Colour online) Spanwise vorticity contours ($\omega_z R/U_{rg}$) at 50 % span for positively cambered wings at $Re = 1500$: (*a*) 0 %, (*b*) 5 %, (*c*) 10 %, (*d*) 15 % ($p/c = 0.5$). The images show flow structures at $\phi = 270°$.

the spanwise vorticity patterns in the chordwise direction where vortices A and B have formed. This is as a result of these streamwise structures interacting with LEV 2 as they begin to dominate the flow. The spanwise vorticity contours in figure 8 show that this interaction results in LEV 2 reducing in size and strength with increased camber, and appears to be confined to the inner part of the wing at high magnitudes of camber.

In an earlier study, Du & Sun (2008) compare the spanwise vorticity patterns of a flat wing to a 10 % cambered wing at 50 % span. They suggest that the LEV is distorted by positive wing camber, but details of what this distortion entails is omitted. Figure 9 displays the variation in spanwise vorticity contours at 50 % span with increasing camber for our simulations. Figure 9 shows that the position of the outer extent of the region of negative vorticity is not altered by the increase in wing camber, and as such the downstream LEV is 'squashed' between the wing's surface and the free stream flow, as shown by the reduction in size of the vortex with increasing camber. Figure 9 demonstrates that even at high magnitudes of camber at this angle of attack the flow still separates from the leading edge. The flow then reattaches to the wing just downstream of the LEV but separates again near the trailing edge for highly cambered wings.

In addition to the change in vorticity patterns, the spanwise velocity distribution over the wing is also influenced by the wing's camber, as is shown by figure 10. For a flat non-cambered wing at a Reynolds number of 1400, Birch *et al.* (2004) found that a strong spanwise velocity existed within the core of the LEV as well as a broad region of moderate spanwise velocity behind it. This can also be seen in our simulations (figure 10*a*). The velocity within the core of LEV 2 reaches a maximum value of

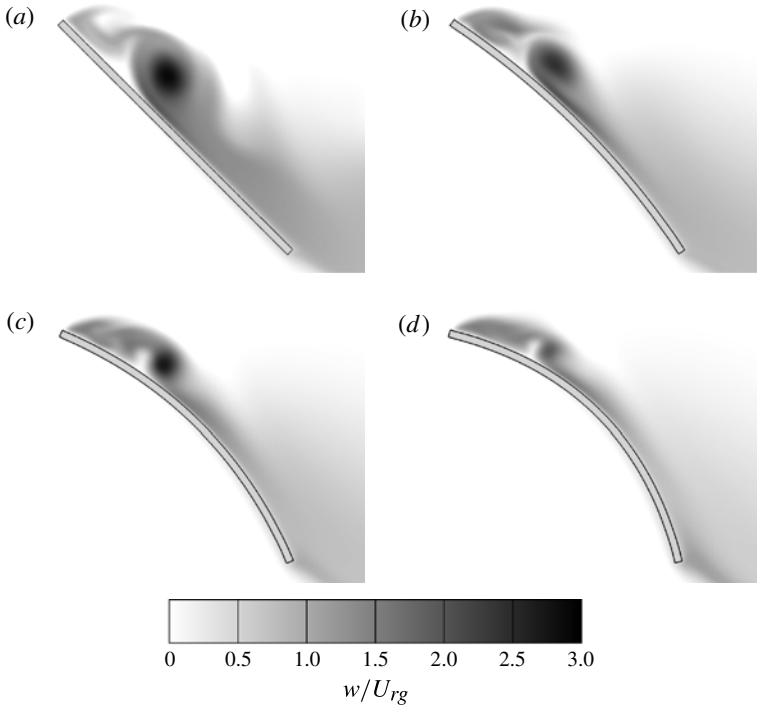

FIGURE 10. Change in spanwise velocity (w/U_{rg}) at 50 % span for positively cambered wings at $Re = 1500$: (*a*) 0 %, (*b*) 5 %, (*c*) 10 %, (*d*) 15 % ($p/c = 0.5$). The images show the velocity contours at $\phi = 270°$.

around three times the velocity at the radius of gyration. This spanwise velocity is thought to help stabilize the LEV to the wing's surface by draining circulation out into the tip vortex (Ellington *et al.* 1996; Lentink & Dickinson 2009). However, figure 10 shows that as the wing's camber is increased the strength of the spanwise velocity within the LEV reduces. Nonetheless, highly cambered wings still have some spanwise velocity (of the order of the velocity at the radius of gyration) near the wing's leading edge where the LEV structures exist, and this appears to be sufficient in maintaining the attachment of the streamwise vortex structures that have formed. Figure 7 shows that these structures still drain into the tip vortex and, as will be shown below, a quasi-steady state is still reached for highly cambered wings.

The development of the vortex structures over a 15 % cambered wing throughout the simulation is shown in figure 11 (see also supplementary movie 3). The initial temporal evolution of the vortex structures over the wing is the same as that for a non-cambered or negatively cambered wing, where a horseshoe-shaped vortex is formed around the wing's edge. As the wing continues to rotate the LEV grows in size and the trailing edge vortex is shed from the wing. However, at $t/T = 0.267$, as the dual LEV begins to form, the iso-Q surface representing LEV 2 becomes rippled, particularly near the wing tip, indicating that the streamwise vortex structures are beginning to form and are being entrained into LEV 2. By $t/T = 0.363$ the aerodynamic forces have reached an approximately steady value as shown in figure 2,

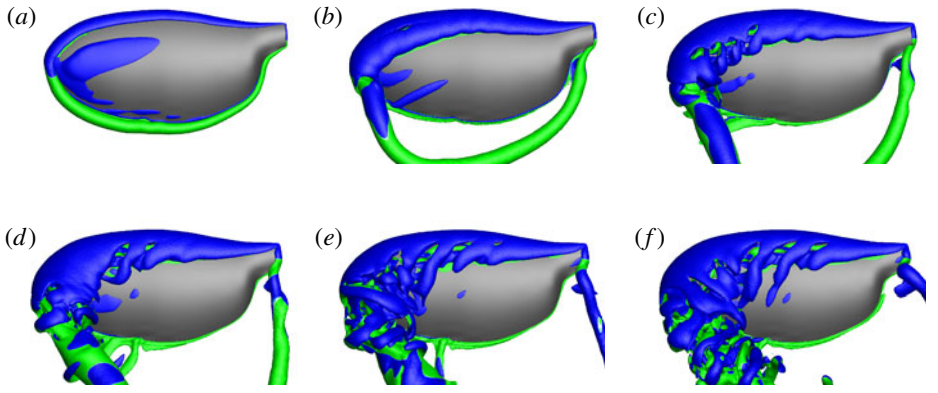

FIGURE 11. (Colour online) Temporal vortex structure development over a 15 % camber wing ($p/c = 0.5, Re = 1500$): (*a*) $t/T = 0.081$, $\phi = 11.1°$; (*b*) $t/T = 0.178$, $\phi = 38.3°$; (*c*) $t/T = 0.267$, $\phi = 63.3°$; (*d*) $t/T = 0.363$, $\phi = 90.5°$; (*e*) $t/T = 0.467$, $\phi = 120°$; (*f*) $t/T = 0.681$, $\phi = 180°$. Vortex structures are visualized using surfaces of constant Q criterion and are coloured by spanwise vorticity (ω_z) to indicate direction: blue is negative and green is positive. The images show flow structures throughout the wing's rotation and are taken perpendicular to the wing's surface.

and yet the vortex structures over the wing continue to develop. Here the streamwise vortices have strengthened further and begin to inhibit the development of LEV 2 across the wing. At $t/T = 0.467$ the three streamwise vortex structures can be seen. Comparison of figure 7(*d*) with figure 11 shows that a quasi-steady vortex system is established over the wing by approximately $t/T = 0.467$ or after 120° of rotation.

3.2.3. *Location of maximum camber*

The chordwise location of maximum camber was found to have a relatively minor impact on the LEV's structure compared to the magnitude of camber. For both positively and negatively cambered wings, the influence of the chordwise location of camber was found to be similar to varying the magnitude of camber but with a more subtle impact on the flow structures.

An example of this is shown in figure 12, which shows the variation in the spanwise vorticity contours for three different positions of maximum camber for a −15 % cambered wing. Figure 12 shows that the dual LEV structure remains persistent between $0.25 \leqslant p/c \leqslant 0.75$. There is, however, a slight variation in the breakdown location of LEV 2, which is more clearly shown in figure 5. Figure 5 shows that moving the location of maximum camber towards the trailing edge of the wing moves the breakdown location towards the wing tip. This effect is similar to reducing the magnitude of negative camber and may be due to the reduction in curvature near the leading edge of the wing seen in both instances.

Similarly, for positively cambered wings moving the location of maximum camber towards the trailing edge was found to be akin to reducing the magnitude of positive camber slightly. This can be seen from figure 13 which shows the variation in iso-surfaces of the Q criterion with the location of maximum camber for a 15 % camber wing. Figure 13 shows that for $p/c = 0.5$ the development of the streamwise vortex structures is such that they limit the development of LEV 2 across the wing's span. However, for $p/c = 0.75$ the development of LEV 2 is not inhibited and it extends further across the wing. This flow structure state is similar to a 10 % camber,

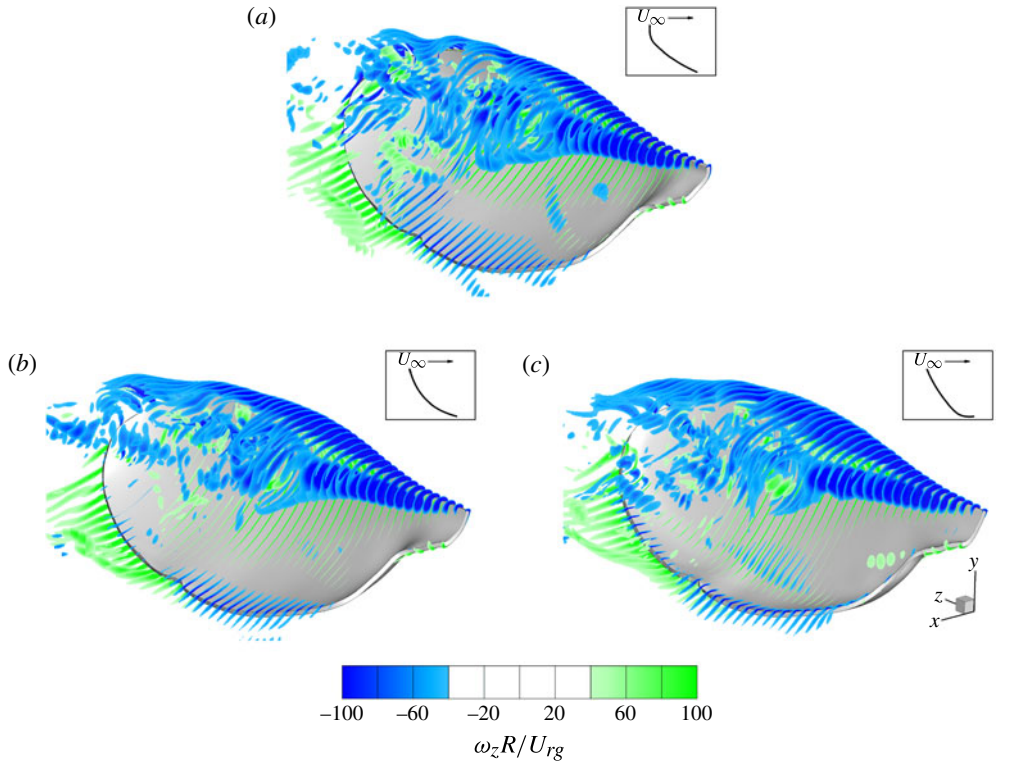

FIGURE 12. (Colour online) Change of spanwise vorticity contours ($\omega_z R/U_{rg}$) with chordwise location of maximum camber for a negatively cambered wing at $Re = 1500$: (*a*) 25 %, (*b*) 50 %, (*c*) 75 % ($m/c = -0.15$). The images show flow structures at $\phi = 270°$. The insets show a cross-sectional view of the wing's shape.

$p/c = 0.5$ wing as shown in figure 7(*c*). In addition, moving the location of maximum camber towards the leading edge (figure 13*a*) results in the streamwise structures moving towards the wing root, which is also seen for a 20 % camber $p/c = 0.5$ wing.

3.3. *Relationship between forces, flow structures and wing camber*

In §§ 3.2.1 and 3.2.2 above, we showed that positively and negatively cambered wings produce very different vortex structures. Despite negatively cambered wings maintaining a strong coherent LEV structure they produce less lift and more drag than a flat wing. On the other hand, highly positively cambered wings have increased aerodynamic performance but do not generate a strong coherent LEV. In this section we explore how wing camber influences the aerodynamic performance of the wing.

For a conventional aircraft wing, which requires attached flow in order to operate, camber is beneficial as it increases the lift coefficient for a given angle of attack over the linear range of the lift coefficient versus angle of attack curve. Usherwood & Ellington (2002) argue that conventional reasoning for camber is flawed for thin flapping and rotating wings at high angles of attack as the flow separates from the wing's leading edge. Therefore an alternative explanation must be found. Usherwood & Ellington (2002) also demonstrate that for these wings the pressure force dominates and consequently the resultant force on a flat wing acts perpendicular to the wing's

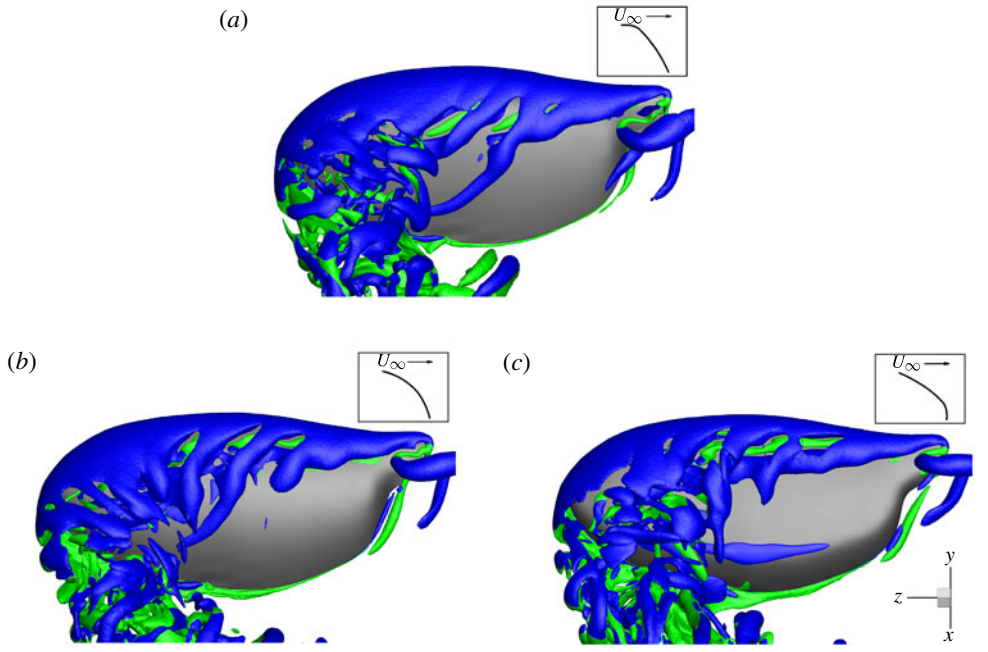

FIGURE 13. (Colour online) Change of vortex structures with chordwise location of maximum camber for a positively cambered wing at $Re = 1500$: (*a*) 25 %, (*b*) 50 %, (*c*) 75 % ($m/c = 0.15$). Vortex structures are visualized using surfaces of constant Q criterion and are coloured by spanwise vorticity (ω_z) to indicate direction: blue is negative and green is positive. The images show flow structures at 270° of rotation and are taken perpendicular to the wing's surface.

surface. This is further explored by Birch *et al.* (2004), who show that at a Reynolds number of 1400 the angle of the net force vector to the wing's surface quickly reaches 90° as the angle of attack of the wing is increased from 0°. This state is reached more slowly at a Reynolds number of 120 due to the added skin friction force.

For our simulations, at a Reynolds number of 1500, the skin friction force makes up between 0.26 and 1.3 % of the total aerodynamic force and therefore the pressure force does indeed dominate. Therefore, a flat wing at a 45° angle of attack should have a lift on drag ratio of approximately one. Figure 3(*b*) shows that the lift on drag ratio for a flat wing is 1.08. This slightly elevated lift on drag ratio is due to low pressure acting across the wing's thickness at the leading edge. Hence, leading edge suction is not insignificant and makes up 3.97 % of the wing's overall force.

In order to explain how increasing camber improves the aerodynamic performance of the wing we first need to look at the pressure distribution over the wing. This is shown in figure 14 for the −15, 0 and 15 % camber wings. Figure 14(*b*) shows that for a flat wing from about the wing's root up until approximately 60 % span there is an intense region of low pressure near the wing's leading edge, which is associated with the proximity of a strong coherent LEV to the wing's surface. Below this region the pressure rapidly increases and thus the wing does not produce much lift (or drag) in this area. Beyond 60 % span, after LEV 2 has burst, the chordwise variation in surface pressure evens out across the wing. Figure 14(*a*) shows that this general description for the surface pressure remains the same for negatively cambered wings except that

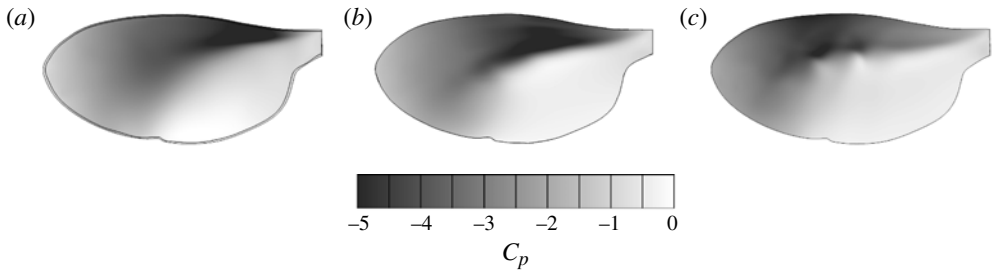

FIGURE 14. Average surface pressure coefficients on the top surface for (*a*) $m/c = -0.15$, (*b*) $m/c = 0$ and (*c*) $m/c = 0.15$ wings ($p/c = 0.5$, $Re = 1500$). Surface pressures have been averaged over the quasi-steady period.

the pressure distribution begins to even out earlier along the span due to the earlier breakdown of LEV 2. For positively cambered wings it can be seen that the intense region of low pressure moves to the outer part of the wing due to the formation of the streamwise vortex structures and consequently there is an increase in pressure over the inner portion of the wing near the leading edge as LEV 2 reduces in strength. However, figure 14 shows that for all wings the majority of the pressure force is produced in the first half of the wing's chord.

The effect of wing camber can then be understood by considering the chordwise pressure distribution on the wing and its relation to the wing's curvature. This is shown in figure 15 for the −15, 0 and 15 % camber wings at 25, 50 and 75 % wing span. Over the inner portion of the wing (e.g. $r/R = 25$ and 50 %) most of the force due to surface pressure is produced near the wing's leading edge. Positively cambered wings have surfaces which are flatter with respect to the horizontal in this portion of the wing. This allows the pressure force to act more vertically in this region, resulting in an upward tilting of the net force vector. Conversely, negatively cambered wings cause this region of low pressure to act more horizontally, lowering the net force vector and therefore reducing lift and increasing drag. In the outer part of the wing, where the pressure distribution is more even across the wing's chord, the effect of camber is minimal as the curvature of the wing near the leading edge is balanced out by the curvature near the trailing edge. This results in an angle of the net force vector to the wing's chord line of approximately 90° for all wings in this region. Therefore, positive wing camber allows the wing to produce lift more effectively over the inner portion of the wing, which consequently improves the wing's overall aerodynamic performance. The reduced suction near the wing's root due to the reduction in LEV 2's strength is outweighed by the effect of the wing's curvature and the formation of streamwise vortices lowers the surface pressure further out along the wing's span, aiding in lift production.

3.4. *Correlation between wing camber and net force coefficient*

In an earlier rotating wing experiment, Zhao *et al.* (2011*a*,*b*) hypothesized that trailing edge flexion directly influences leading edge vorticity and consequently the magnitude of the aerodynamic forces on flexible wings. Their experiment consisted of a flexible wing rotating at a constant rotational velocity. The leading edge of the wing was fixed at an angle of attack of 45° while the rest of the wing was free to deform. They found that as the wing's flexural stiffness was reduced, the wing bent into a negatively cambered shape and there was a reduction in net force coefficient. The degree of wing

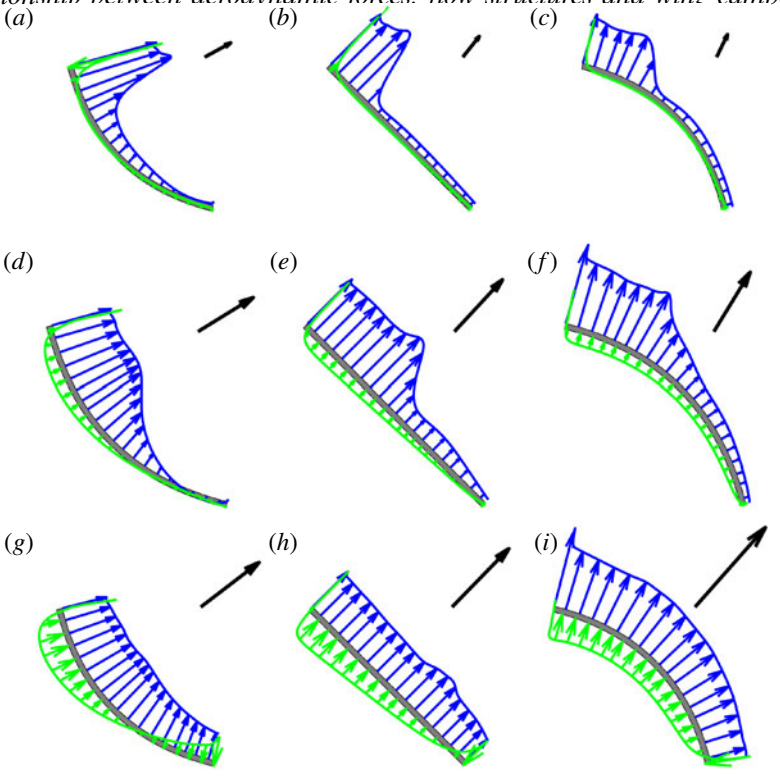

FIGURE 15. (Colour online) Force vectors due to surface pressure distribution at three spanwise locations for $m/c = -0.15$, 0 and 0.15 camber wings ($p/c = 0.5$, $Re = 1500$): (*a–c*) $r/R = 0.25$, (*d–f*) $r/R = 0.50$, (*g–i*) $r/R = 0.75$; (*a,d,g*) -15 %, (*b,e,h*) 0 % and (*c,f,i*) 15 % camber. The upper surface vectors are shown in blue and the lower surface vectors in green. The leading and trailing edge vectors are not shown. The black arrow is the scaled net force vector for that cross-section.

deformation was measured as wing flexion, which they defined as the angle between the leading edge tangent and the trailing edge tangent. Their data has been reproduced in figure 16.

To compare our data, we calculated the flexion angle and the net force coefficient for our cambered wings. The net force coefficient was calculated as $C_F = 2F/\rho U_{rg}^2 S$, where F is the net aerodynamic force. As shown in figure 3, we found that increasing the magnitude of negative wing camber results in a reduction in lift coefficient but an increase in drag coefficient. This corresponds to a roughly constant net force coefficient with increasing flexion (figure 16). Our data shows just a 4.6 % drop in the net force coefficient from 0 to $-60°$ of flexion. These findings are markedly different from those of Zhao *et al.* (2011*a*,*b*), who found a 68.8 % drop in the net force coefficient between 0 and $-40°$ of flexion.

A possible explanation for this difference in trends could be a change in the wing's angle of attack in the experiments. Previous studies that have investigated the effect of angle of attack have shown that the net force reduces with decreasing angle of attack (Dickinson *et al.* 1999; Usherwood & Ellington 2002; Birch *et al.* 2004). In our simulations we keep the angle of attack (angle between the mean chord line and the free stream flow) constant as the wing's camber is varied, while Zhao *et al.* (2011*a*,*b*)

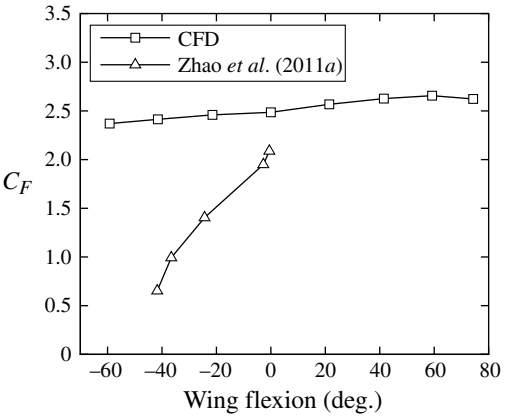

FIGURE 16. Variation of net force coefficient with wing flexion. Negative wing flexion corresponds to negative wing camber while positive wing flexion is positive wing camber. Comparison to experimental data from Zhao *et al.* (2011*a*).

fix the leading edge angle and allow the wing's trailing edge to deform to the flow. Consequently, the angle of attack of the wing reduces as the wing flexes and their data therefore include a change in angle of attack as well as a change in wing shape. It is therefore likely that their results are dominated by the reduction in angle of attack experienced by the wing and are not due to the change in wing camber. Our results show that there is only a weak correlation between wing camber and the magnitude of the net aerodynamic force.

3.5. *Effect of camber at low Reynolds numbers*

It is well known that the characteristics of the LEV change with Reynolds number. Birch *et al.* (2004) showed that at a Reynolds number of 1400 the LEV forms a tight spiral structure with a strong axial velocity in its core, but at a Reynolds number of 120 it does not. Ellington *et al.* (1996) reported a similar conical spiral LEV with an intense spanwise flow within its core for hovering hawkmoth flight ($Re \approx 5000$), while Shyy & Liu (2007) and Liu & Aono (2009) reported a similar change in the LEV's structure between a hovering fruit fly ($Re = 134$), honeybee ($Re = 1123$) and hawkmoth ($Re = 6300$) using a computational model. Lu *et al.* (2006) found that for Reynolds numbers greater than 640 a dual co-rotating LEV structure forms in which the primary vortex has a tight spiral structure. As shown in § 3.2, this dual LEV structure is also seen in our simulations and both the breakdown point of LEV 2 and the point along the span at which a clear dual vortex structure can first be seen have been shown to be dependent on the span-based Reynolds number (Harbig *et al.* 2013).

The results of this study were performed at a Reynolds number of 1500 where a clear dual LEV structure exists for a flat wing. The above literature shows that the LEV's structure does not change greatly for Reynolds numbers higher than this, and therefore the effect of wing camber should be similar. However, at lower Reynolds numbers the LEV's structure does change significantly and therefore the effect of camber at these Reynolds numbers needs to be explored. We therefore briefly investigate how camber affects the wing's performance and flow structures at a Reynolds number of 120.

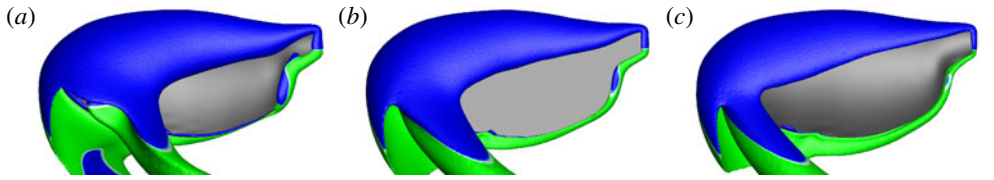

FIGURE 17. (Colour online) Vortex structures at $Re = 120$ for (*a*) $-15\,\%$, (*b*) $0\,\%$ and (*c*) $15\,\%$ camber ($p/c = 0.5$). Vortices are visualized using surfaces of constant Q criterion and are coloured by spanwise vorticity (ω_z) to indicate direction: blue is negative and green is positive. The images show flow structures at $\phi = 270°$ and are taken perpendicular to the wing's surface.

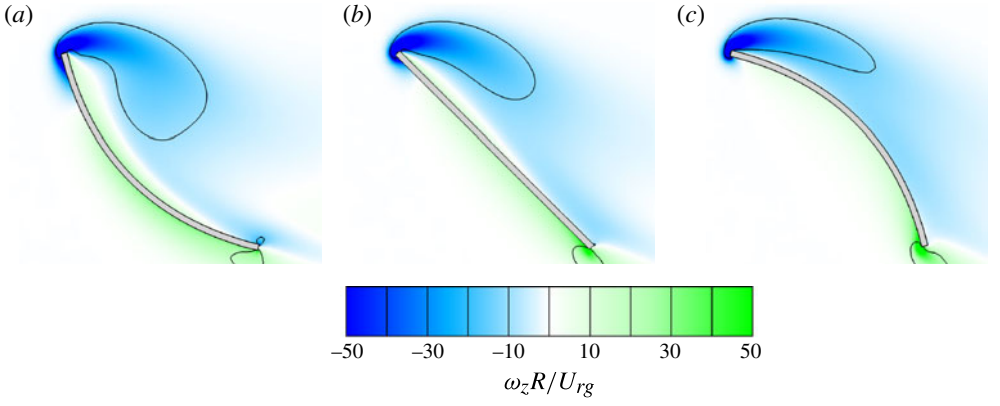

FIGURE 18. (Colour online) Spanwise vorticity contours ($\omega_z R/U_{rg}$) at $50\,\%$ span for (*a*) $-15\,\%$, (*b*) $0\,\%$ and (*c*) $15\,\%$ camber wings ($p/c = 0.5$) at $Re = 120$. Solid black lines represent a contour of the Q criterion of the same value as the iso-surfaces shown in figure 17. The images show flow structures at $\phi = 270°$.

The variation in the vortex structures between Reynolds numbers of 120 and 1500 for a flat wing has been previously reported in Harbig *et al.* (2013) and is consistent with the observations described above. At this low Reynolds number ($Re = 120$) a single, less intense, LEV forms over the wing with reduced spanwise velocity in its core. Unlike at higher Reynolds numbers, here only minor changes in the LEV's structure are seen for both positive and negative camber. Figure 17 shows iso-surfaces of the Q criterion over -15, 0 and $15\,\%$ camber wings. A similar vortex system is seen for all wings where the single LEV extends across the wing and connects with the tip vortex. A trailing edge vortex forms and is seen to remain attached to the wing, only separating from the wing near the wing tip, outside the tip vortex, thus forming a pair of counter-rotating vortices in the wake. This vortex structure was also observed by Poelma *et al.* (2006) in their particle image velocimetry experiments on a revolving fruit fly wing.

One change that can be seen with camber is that the tip vortex moves outboard slightly with increasing camber. The LEV also becomes compressed with increased camber, which is shown in figure 18 by the black line representing a contour of the Q criterion. At $-15\,\%$ camber the LEV is fuller and more rounded, but as the camber is increased the LEV becomes elongated in the streamwise direction.

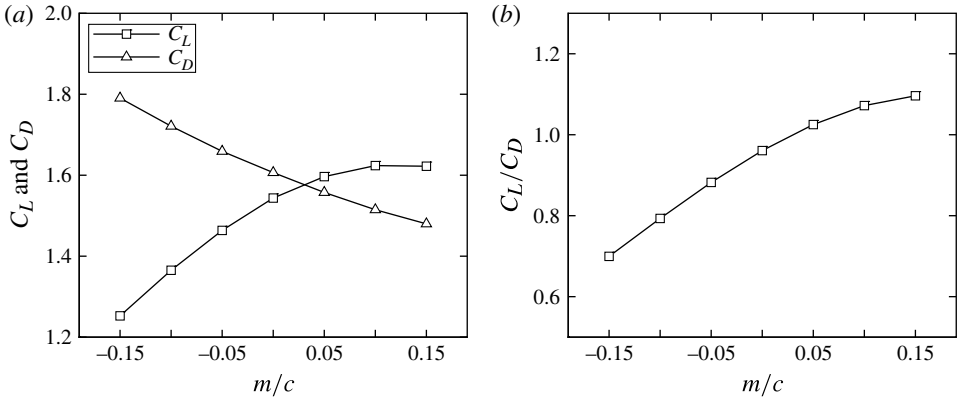

FIGURE 19. Average aerodynamic force graphs at $Re = 120$. (*a*) Change in lift and drag coefficients with magnitude of camber, m/c ($p/c = 0.5$). (*b*) Variation in lift on drag ratio with magnitude of camber.

Despite the lack of a significant change in the LEV's structure with camber, a substantial increase in the wing's performance is still seen for positively cambered wings. The variation in aerodynamic forces with camber at a Reynolds number of 120 is shown in figure 19 and shows that a similar increase in lift coefficient and a decrease in drag coefficient are seen with increasing camber as was seen at the higher Reynolds number. Here we found a 14 % increase in the lift on drag ratio at 15 % camber compared to a flat wing. This percentage increase is about half that at $Re = 1500$, which shows that camber has a reduced effect at lower Reynolds numbers. A decreased benefit of positive camber at lower Reynolds numbers was also found by Du & Sun (2008) for a flapping wing.

The mechanism through which camber improves the wing's performance is the same at $Re = 120$ as it is at $Re = 1500$. The pressure force still dominates, making up between 94 and 99 % of the total aerodynamic force depending on the magnitude of camber and, while weaker, the LEV still produces a region of lower pressure near the leading edge of the wing. Thus increasing the wing's camber allows this low pressure to act more vertically, which results in a tilting of the net force vector (figure 20). In fact the net force coefficient varies by less than 2 % between −15 % and 15 % wing camber at this Reynolds number, and therefore the variation in lift and drag coefficients that are seen are purely due to the angling of the net force vector and not from a change in its magnitude.

4. Conclusion

In this paper we have investigated the aerodynamic forces and flow structures that are produced by stiff cambered rotating insect wings by solving the Navier–Stokes equations cast in a rotating reference frame. These simulations were calculated at Reynolds numbers of 120 and 1500 and both the magnitude and the chordwise location of maximum camber were examined.

At a Reynolds number of 1500, a flat non-cambered wing produces a dual LEV structure which consists of two co-rotating spanwise oriented vortex structures that are separated by a smaller counter-rotating vortex. It was found that negatively cambered

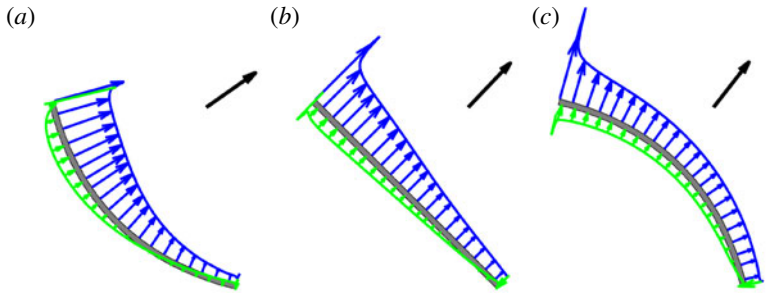

FIGURE 20. (Colour online) Force vectors due to surface pressure distribution at 50 % span for $m/c = -0.15$, 0 and 0.15 camber wings ($p/c = 0.5$) at $Re = 120$: (*a*) -15 %, (*b*) 0 % and (*c*) 15 % camber. The upper surface vectors are shown in blue and the lower surface vectors in green. The leading and trailing edge vectors are not shown. The black arrow is the scaled net force vector for that cross-section.

wings maintain this dual LEV structure, but the wing's concave shape allows the downstream vortex to break down earlier along the wing's span.

On the other hand, positively cambered wings produce very different LEV structures to flat or negatively cambered wings. Here an increase in wing camber results in multiple streamwise vortex structures forming at the leading edge. Initially these structures are weak and are entrained into the main LEV, but as the wing's camber is increased they begin to dominate the flow and prevent the dual LEV structure from developing across the wing's span. Despite a reduction in the magnitude of spanwise velocity, corresponding to the degradation of the main LEV, a significant spanwise velocity still exists for highly positively cambered wings. This allows the streamwise vortices to feed into the tip vortex, and as such a quasi-steady state is still reached for these wings.

For both positively and negatively cambered wings, the influence of the chordwise location of camber was found to be akin to varying the magnitude of camber but with a more subtle impact on the flow structures. Moving the location of maximum camber towards the trailing edge of the wing produced similar changes in flow structures to reducing the magnitude of positive or negative camber, which was attributed to the associated reduction in curvature near the leading edge of the wing.

Our simulations showed that positively cambered wings produce higher lift coefficients and lower drag coefficients compared to flat or negatively cambered wings. While we found that aerodynamic performance was still improving at 20 % camber, this magnitude of camber is likely to be beyond what is typically observed in insect flight. However, our results show that even a small increase in wing camber would result in a significant improvement in aerodynamic performance for insects. Moreover, micro air vehicle designers may wish to use more aggressive camber to exploit its benefits.

The relationship between the flow structures and the aerodynamic forces was also assessed. It was found that both positively and negatively cambered wings produce chordwise pressure distributions that have a region of low pressure near the leading edge for most of the wing's span. This pressure distribution combined with the curvature near the leading edge results in a tilting of the net force vector, either more vertically for positive camber or more horizontally for negative camber, which leads

to the variation in aerodynamic forces that are seen. This improved understanding explains why insects can benefit from wing camber.

The effect of camber at a Reynolds number of 120 was also investigated. It was found that at this Reynolds number only minor changes in the LEV's structure were observed, but an improvement in the wing's lift on drag ratio was still obtained for positively cambered wings. It was shown that it is the same mechanism (the pressure distribution combined with the wing's curvature) that acts to improve aerodynamic performance at this low Reynolds number as at a Reynolds number of 1500. Therefore camber is beneficial for flapping and rotating wings at Reynolds numbers between 120 and 1500, and possibly higher.

Acknowledgements

This research was undertaken with the assistance of resources provided at the Australian National University through the National Computational Merit Allocation Scheme supported by the Australian Government.

Supplementary movies

Supplementary movies are available at http://dx.doi.org/10.1017/jfm.2013.335.

REFERENCES

ALTSHULER, D. L., DUDLEY, R. & ELLINGTON, C. P. 2004 Aerodynamic forces of revolving hummingbird wings and wing models. *J. Zoology* **264**, 327–332.

AONO, H., LIANG, F. & LIU, H. 2008 Near- and far-field aerodynamics in insect hovering flight: an integrated computational study. *J. Expl Biol.* **211**, 239–257.

BIRCH, J. M. & DICKINSON, M. H. 2001 Spanwise flow and the attachment of the leading-edge vortex on insect wings. *Nature* **412**, 729–733.

BIRCH, J. M., DICKSON, W. B. & DICKINSON, M. H. 2004 Force production and flow structure of the leading edge vortex on flapping wings at high and low Reynolds numbers. *J. Expl Biol.* **207** (7), 1063–1072.

DICKINSON, M. H. & GOTZ, K. G. 1993 Unsteady aerodynamic performance of model wings at low Reynolds numbers. *J. Expl Biol.* **174** (1), 45–65.

DICKINSON, M. H., LEHMANN, F.-O. & SANE, S. P. 1999 Wing rotation and the aerodynamic basis of insect flight. *Science* **284** (5422), 1954–1960.

DU, G. & SUN, M. 2008 Effects of unsteady deformation of flapping wing on its aerodynamic forces. *Z. Angew. Math. Mech.: Appl. Math. Mech.* **29** (6), 731–743.

ELLINGTON, C. P. 1984 The aerodynamics of hovering insect flight. Part 3. Kinematics. *Phil. Trans. R. Soc.* B: *Biol. Sci.* **305** (1122), 41–78.

ELLINGTON, C. P., VAN DEN BERG, C., WILLMOTT, A. P. & THOMAS, A. L. R. 1996 Leading-edge vortices in insect flight. *Nature* **384** (19), 626–630.

GOPALAKRISHNAN, P. & TAFTI, D. K. 2010 Effect of wing flexibility on lift and thrust production in flapping flight. *AIAA J.* **48** (5), 865–877.

HALL, M. G. 1972 Vortex breakdown. *Annu. Rev. Fluid Mech.* **4** (1), 195–218.

HARBIG, R. R., SHERIDAN, J. & THOMPSON, M. C. 2013 Reynolds number and aspect ratio effects on the leading-edge vortex for rotating insect wing planforms. *J. Fluid Mech.* **717**, 166–192.

HUNT, J. C. R., WRAY, A. A. & MOIN, P. 1988 Eddies, streams, and convergence zones in turbulent flows. Center for Turbulence Research *Tech. Rep.* CTR-S88.

JENSEN, M. 1956 Biology and physics of locust flight. Part 3. The aerodynamics of locust flight. *Phil. Trans. R. Soc.* B: *Biol. Sci.* **239** (667), 511–552.

KWEON, J. & CHOI, H. 2010 Sectional lift coefficient of a flapping wing in hovering motion. *Phys. Fluids* **22** (7), 071703.

LENTINK, D. & DICKINSON, M. H. 2009 Rotational accelerations stabilize leading edge vortices on revolving fly wings. *J. Expl Biol.* **212** (16), 2705–2719.

LIU, H. & AONO, H. 2009 Size effects on insect hovering aerodynamics: an integrated computational study. *Bioinspir. Biomim.* **4**, 015002.

LU, Y., SHEN, G. X. & LAI, G. J. 2006 Dual leading-edge vortices on flapping wings. *J. Expl Biol.* **209**, 5005–5016.

NAKATA, T. & LIU, H. 2012*a* A fluid–structure interaction model of insect flight with flexible wings. *J. Comput. Phys.* **231** (4), 1822–1847.

NAKATA, T. & LIU, H. 2012*b* Aerodynamic performance of a hovering hawkmoth with flexible wings: a computational approach. *Proc. R. Soc.* B: *Biol. Sci.* **279** (1729), 722–731.

PHILLIPS, N., KNOWLES, K. & LAWSON, N. J. 2010 Effect of wing planform shape on the flow structures of an insect-like flapping wing in hover. In *27th Inernational Congress of the Aeronautical Sciences, 19–24 September 2010, Nice, France. Paper ICAS* 2010-6.10.4. http://www.icas.org/ICAS_ARCHIVE/ICAS2010/ABSTRACTS/260.HTM.

POELMA, C., DICKSON, W. B. & DICKINSON, M. H. 2006 Time-resolved reconstruction of the full velocity field around a dynamically-scaled flapping wing. *Exp. Fluids* **41** (2), 213–225.

ROACHE, P. J. 1998 Verification of codes and calculations. *AIAA J.* **36** (5), 696–702.

SHYY, W. & LIU, H. 2007 Flapping wings and aerodynamic lift: the role of leading-edge vortices. *AIAA J.* **45** (12), 2817–2819.

SRYGLEY, R. B. & THOMAS, A. L. R. 2002 Unconventional lift-generating mechanisms in free-flying butterflies. *Nature* **420**, 660–664.

TSUZUKI, N., SATO, S. & ABE, T. 2007 Design guidelines of rotary wings in hover for insect-scale micro air vehicle applications. *J. Aircraft* **44** (1), 252–263.

USHERWOOD, J. R. & ELLINGTON, C. P. 2002 The aerodynamics of revolving wings. Part 1. Model hawkmoth wings. *J. Expl Biol.* **205** (11), 1547–1564.

VOGEL, S 1967 Flight in *Drosophila*. Part 3. Aerodynamic characteristics of fly wings and wing models. *J. Expl Biol.* **46**, 431–443.

WALKER, S. M., THOMAS, A. L. R. & TAYLOR, G. K. 2009 Deformable wing kinematics in the desert locust: how and why do camber, twist and topography vary through the stroke? *J. R. Soc.: Interface* **6** (38), 735–747.

WALKER, S. M., THOMAS, A. L. R. & TAYLOR, G. K. 2010 Deformable wing kinematics in free-flying hoverflies. *J. R. Soc.: Interface* **7** (42), 131–142.

WEIS-FOGH, T. 1973 Quick estimates of flight fitness in hovering animals, including novel mechanisms for lift production. *J. Expl Biol.* **59**, 169–230.

WOOTTON, R. J. 1981 Support and deformability in insect wings. *J. Zoology* **193**, 447–468.

YOUNG, J., WALKER, S. M., BOMPHREY, R. J., TAYLOR, G. K. & THOMAS, A. L. R. 2009 Details of insect wing design and deformation enhance aerodynamic function and flight efficiency. *Science* **325** (5947), 1549–1552.

ZANKER, J. M. & GOTZ, K. G. 1990 The wing beat of *Drosophila melanogaster*. Part 2. Dynamics. *Phil. Trans. R. Soc.* B: *Biol. Sci.* **327**, 19–44.

ZHAO, L., DENG, X. & SANE, S. P. 2011*a* Modulation of leading edge vorticity and aerodynamic forces in flexible flapping wings. *Bioinspir. Biomim.* **6** (3), 036007.

ZHAO, L., DENG, X. & SANE, S. P. 2011*b* Trailing edge flexion influences leading edge vortices and aerodynamic forces in flapping wings. In *49th AIAA Aerospace Sciences Meeting, 4–7 January 2011, Orlando, Florida. Paper AIAA* 2011-1310.

ZHAO, L., HUANG, Q., DENG, X. & SANE, S. P. 2010 Aerodynamic effects of flexibility in flapping wings. *J. R. Soc.: Interface* **7** (44), 485–497.